Coastal Dynamics 2017
Paper No. 127

SURF ZONE MORPHODYNAMICS DURING LOW-MODERATE ENERGETIC CONDITIONS; THE TASTI FIELD EXPERIMENT

Joost Brinkkemper[1], Drude Christensen[2], Timothy Price[1], Ivo Naus[1], Asger Hansen[3], Vera van Bergeijk[1], Johnny van de Wetering[1], Gerben Ruessink[1], Verner B. Ernstsen[2] and Troels Aagaard[2]

Abstract

During low-moderate energetic conditions, onshore migration of intertidal bars results in beach accretion. The mechanisms driving the onshore directed transport of sand and their relative importance are still under debate. To improve our knowledge on these mechanisms, a field experiment was conducted at the beach of Vejers, Denmark. Measurements of flow velocities including turbulence, sand concentrations and morphology were collected in the intertidal zone for a period of four weeks. This resulted in a unique dataset including detailed measurements at multiple locations during two periods with an onshore migrating intertidal bar. This paper gives an insight in the type of measurements that were collected, the hydrodynamic conditions and resulting variability in the cross-shore and alongshore morphology during the campaign, and presents preliminary results.

Key words: turbulence, onshore bar migration, alongshore variability, in-situ measurements

1. Introduction

It is well known that nearshore bars move in the offshore direction during storms and in the onshore direction during low energetic conditions. While the offshore directed sand transport is reasonably well understood and mainly driven by the undertow (e.g., Gallagher et al., 1998), our knowledge on the onshore directed and mainly wave-driven transport is still rather poor (e.g., Van Rijn et al, 2011). The onshore directed transport of sand during fair weather conditions is, however, essential for beach recovery between storms and a better understanding of the processes involved is thus crucial to improve predictions of coastal development.

The onshore directed migration of nearshore bars is often the result of onshore directed short wave-driven transport being larger than the offshore directed transport by the mean cross-shore current at the seaward flank and over the crest of a bar. The onshore directed short-wave transport in the surf zone has before been ascribed to velocity skewness (e.g. Ribberink and Al-Salem, 1994; O'Donoghue and Wright, 2004), acceleration skewness (e.g. Watanabe and Sato, 2004; van der A et al., 2009; Silva et al., 2011) and the surface-induced turbulence beneath plunging breakers (e.g. Aagaard and Hughes, 2010; Brinkkemper et al., 2017). It remains unclear, however, what the relative contributions of these processes are to the migration of nearshore sandbars.

In the alongshore direction, cross-shore migration rates may vary within distances of <200 m, despite identical offshore wave conditions. In this case, alongshore variations in bar depth result in alongshore variable wave fields over the bar, driving horizontal circulation patterns (Falqués et al., 2000). At the shallower parts, if the water depth above the bar crest is small and the trough landward of the bar is sufficiently pronounced (Sunamura and Takeda, 1984; Aagaard et al., 2006; Aagaard and Vinther, 2008), the onshore directed propagation of an intertidal bar results from the short-wave, infragravity-wave and

[1]Department of Physical Geography, Faculty of Geosciences, Utrecht University, Heidelberglaan 2, 3584 CS Utrecht, the Netherlands, j.a.brinkkemper@uu.nl, t.d.price@uu.nl, b.g.ruessink@uu.nl
[2]Institute of Geosciences and Natural Resources, University of Copenhagen, Oster Voldgade 10, DK-1350 Copenhagen K., Denmark, dc@ign.ku.dk, taa@ign.ku.dk
[3]Department of Mechanical Engineering, Technical University of Denmark, Nils Koppels Allé 403, 2800 Kgs. Lyngby, Denmark, asbha@mek.dtu.dk

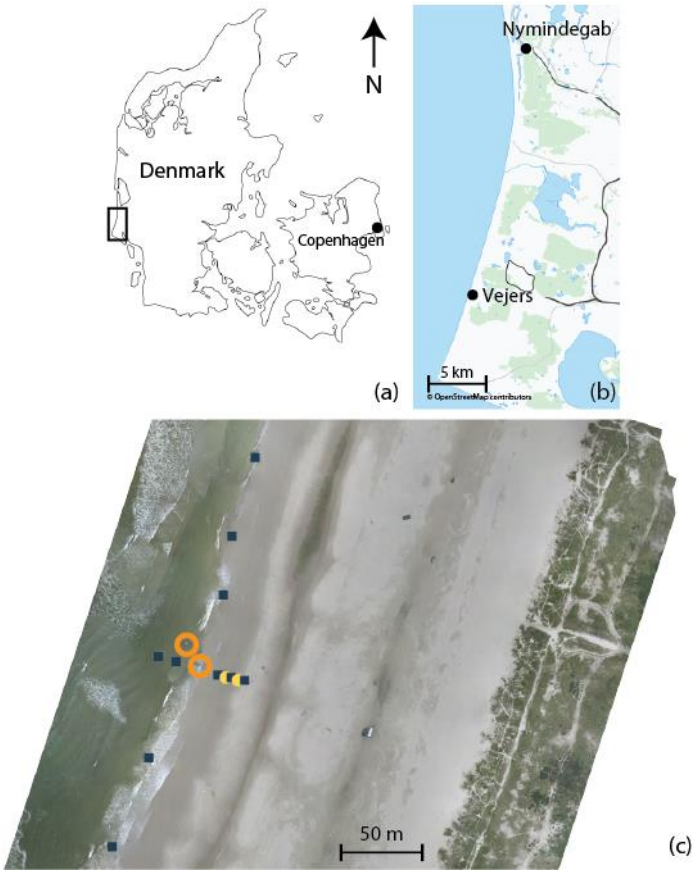

Figure 1. The location of (a) the study area in Denmark, (b) the fieldsite and the waverider buoy at Vejers and Nymindegab, respectively and (c) an orthophoto of the fieldsite. The symbols in (c) indicate the location of the instruments with (orange circles) R1 and R2, (yellow circles) R3 and R4, and (blue squares) the pressure sensors.

mean transport all being onshore-directed. Here, the mean onshore current over the bar crest is compensated by offshore directed rip currents over the deeper parts of the bar crest. The alongshore variability of the intertidal bar may be coupled to that of the subtidal bar (Price et al., 2014). It is hypothesized that the variability in intertidal bar morphodynamics is partly driven by a modulation of the wave height by the alongshore variable water depth over the crescentic subtidal bar crest (Castelle et al., 2010). Field evidence supporting this hypothesis, however, is currently lacking.

To improve our knowledge on the morphodynamics during onshore bar migration and more specifically to determine which mechanisms are responsible for the onshore directed sand transport, the field experiment TASTI (Turbulence And Sand Transport Initiative) was conducted at the beach of Vejers, Denmark in September/October 2016. The experiment resulted in a dataset containing two periods of onshore directed migration of an intertidal bar. In this contribution we first introduce the field experiment (Section 2), followed by some preliminary results (Section 3) and the first conclusions (Section 4).

2. Field experiment

2.1 *Setting*

The field experiment was conducted between September 16 and October 10 in 2016 at the beach near Vejers, Denmark (Figures 1a,b). This beach is characterized by a yearly average offshore significant waveheight of 1.3 m and a mean wave period of 4-5 s, a semidiurnal tide ranging from 0.6 m (neap) to 1.3

m (spring) and at the shoreface a median grain size of 180-200 µm. The nearshore consists of a multiple (3-4) bar system, these bars show a net offshore migration cycle (period in the order of 15 years) and decay in approximately 6 m water depth at a distance of around 900 m from the shoreline (Aagaard and Kroon, 2007). Despite the net offshore bar migration, the beach accretes with a rate of 6-7 $m^3/m/y$ due to a gradient in the net sand transport by wave-driven alongshore currents (Aagaard, 2011). The typical beach width is 150 m and the mean slope of the upper shoreface is 0.006.

There have been field campaigns focusing on longshore bar dynamics and breaking induced turbulence at the beach of Vejers previously (Aagaard and Hughes, 2010; Aagaard and Jensen, 2013). The campaign presented herein, however, is the first at this site to include simultaneous measurements of the vertical profiles of turbulence and sand concentration at multiple locations, and with extensive surveys of both cross-shore and alongshore morphodynamics.

2.2 *Instrumentation*

Instruments were deployed in a cross-shore and alongshore array, mostly within the intertidal zone from -1 to 1 m above mean sea level (Figure 1c). The cross-shore array consisted of five individual pressure transducers (PT; P1 – P5) to estimate water depth and wave characteristics, and four PTs which were collocated with other instruments at the two main rigs (R1 and R2) and two smaller rigs (R3 and R4). The alongshore array was located along the low water line on the first day of the campaign, centred around the cross-shore array, and consisted of five additional PTs (P6 – P10) to measure alongshore differences in the wave field over the intertidal beach. The offshore significant waveheight H_0 was available from a wave buoy near Nymindegab (Figure 1b) in 16 m water depth.

The two main rigs were initially deployed in the trough between the first, most landward located, subtidal bar and the intertidal bar (R1) and at the low water line (R2). Both rigs were equipped with three vertically spaced acoustic current meters (ADVs) to estimate the vertical variability in turbulent fluctuations (Ruessink, 2010) at 10 Hz. Sand concentrations were measured at R1 with five fiber-optical backscatter sensors (UFOBS; Downing, 2006) close to the bed (nominally 0.01-0.05 m) and with three individual optical backscatter sensors (OBS3+) higher in the water column (0.05-0.25 m), at R2 a vertical stack of five OBSs was used for near-bed measurements (nominal height of the sensing volumes 0.04 – 0.17 m above the bed) and two individual OBSs were deployed higher in the water column (0.25 and 0.30 m above the bed). Bedforms were monitored at R1 with an Imagenex 881A Profiling Sonar, scanning in a cross-shore line and an Imagenex 881A Imaging Sonar for 2D imaging of the seabed. At R2 high-resolution circular elevation models were measured every 30 minutes using a 1.1 MHz 3D profiling Sonar 2001 (Marine Electronics Ltd., see also Ruessink et al., 2016). Data loggers and batteries were included in both rigs, R1 additionally uploaded part of the data with a 3G modem connection. While R2 was deployed for the full length of the experiment, R1 was recovered at day 9 because of high rates of local accretion which buried the instruments.

The two smaller rigs (R3 and R4) were deployed between R2 and the high water line. These rigs contained a PT, an electromagnetic flow meter (EMF) to measure horizontal velocities and three vertically spaced OBSs. The nominal height of the PTs was 0.10 m, for the EMFs 0.15 m and for the OBSs 0.05, 0.10 and 0.15 m above the bed. The measurements collected by these instruments were used to estimate transport gradients landward of the two main rigs.

Instrument heights above the bed were measured, and if necessary readjusted, once a day during low tide. The elevation of the intertidal beach was measured with a wheeled RTK GPS carrier over an area alongshore from 150 m north to 150 m south of the instrument array and cross-shore from the top of the primary foredune to approximately -1 m below mean sea level. These surveys were conducted every day

during low tide, except for three days when the water level was too high. To get qualitative data on the position and the alongshore variability of the subtidal bars, a daily time-exposure image was created by recording and averaging images collected for 10 minutes with 2 Hz using a GoPro camera during low-tide from the top of the foredune.

Furthermore, a number of innovative instruments were deployed, for comparison of their measurements with data from more conventional instruments. A SICK LMS511 laser scanner was deployed on day 15 and 16 to measure the instantaneous water surface along the cross-shore instrument array. The scanner was mounted on a 10 m high aluminium tower and set to scan at 25 Hz with an angular resolution of 1/6 degree. The two major advantages over an array of pressure sensors are the high cross-shore resolution and a better approximation of the wave shape in shallow water, as pressure data needs to be converted to the sea surface elevation with for example linear wave theory. Moreover, a tilt current meter (TCM) was deployed at R1 from day 6 until day 9 of the experiment (Hansen et al, 2017). The TCM consisted of a cylindrical floatation body fitted with 9 degree of freedom motion sensor (accelerometer, gyro and compass). The floatation body was tethered to a casing containing a data logger and the energy supply. Using the pre-determined response curve, the measured tilt angles were used to estimate the two horizontal components of the flow velocity. Similar devices were earlier successfully deployed in deeper water to estimate tidal currents (e.g. Radermacher et al., 2015). Measurements of the cross-shore flow velocity by the TCM during the campaign in Vejers shows good agreement with measurements by a collocated ADVO, both for mean currents as for the wave-orbital motion. These results are presented and further discussed by Hansen et al. (2017).

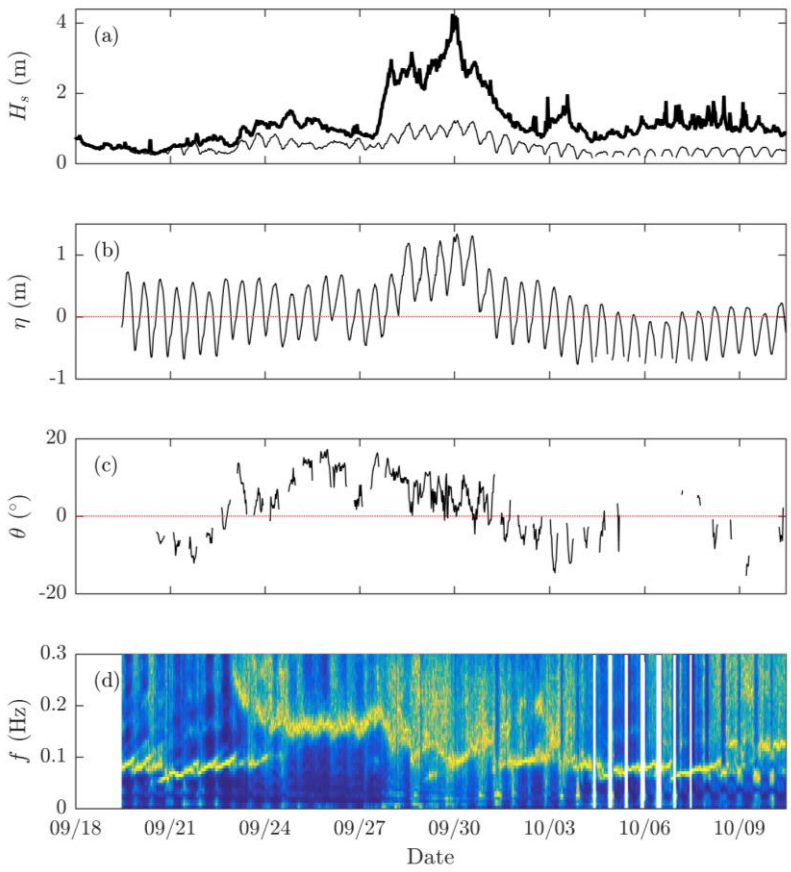

Figure 2. Hydrodynamics during the field campaign, with (a) the significant waveheight H_s at the (bold) offshore wave buoy and at the most seaward pressure sensor P1, (b) the water level η in respect to ordnance datum (DVR90), (c) wave angle of incidence θ at R2 and (d) normalized wave-energy spectra at P1.

2.3 *Wave conditions*

During the first five days of the campaign (September 16 – 21), the offshore wave conditions were characterized by long-period (T_p ~ 12 s) swell waves (H_0 ~ 0.5 m), with the peak wave period T_p gradually decreasing as swell-waves were dispersed while propagating from their distant source (Figures 2a,c). The wave-angle of incidence at R2 in this period was between five and ten degrees North of shore normal (Figure 2b). At September 22 wind from the North West generated waves at higher frequencies and a transition from swell waves to sea waves can be observed in the wave spectrum (Figure 2d). These sea waves with T_p ~ 7 s reached R2 with an angle between 10^o and 15^o South from the shore normal, i.e. from the West (Figure 2c). The waveheight at the most seaward located pressure sensor now shows lower values than the offshore waveheight and waves thus dissipated part of their energy seaward of our instrument array. From the 13th to the 15th day of the experiment (September 29 – October 1), a northwesterly storm resulted in an increase in H_0 to up to 4 m, and elevated waterlevels (Figures 2a,b). The wave angle of incidence at our instrument array decreased as the higher waves were refracted further seaward. The storm was followed by low-energetic swell conditions (H_0 < 1 m) and an easterly wind from day 16 till day 24 (October 2 – October 10). The waveheight at the wave buoy now also includes seaward propagating waves and is thus not representative for the waves at the field site. Limited data could be collected during this period, as the water level was lowered by the offshore directed winds and rarely exceeded the crest of the intertidal bar.

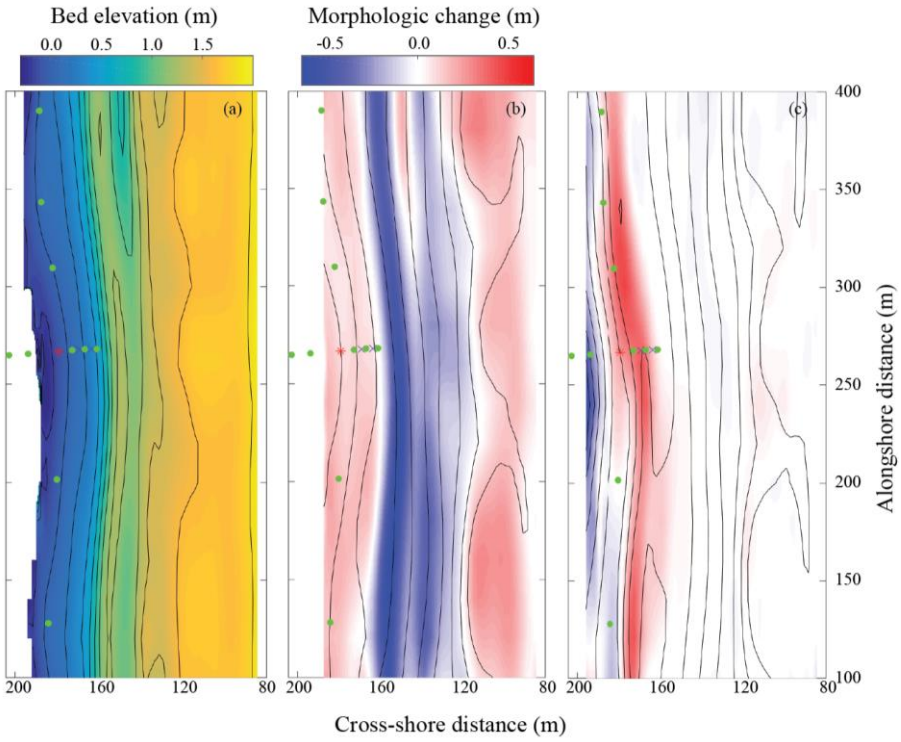

Figure 3. (a) The bed elevation at September 27 (before the storm) with 0.20 m spaced contours, (b) difference between the survey at the September 27 and October 2, the contours indicate bed elevation at October 2, and (c) difference between the survey at October 2 and October 10 with contours showing the bed elevation at October 10. The symbols indicate the locations of (green circles) PTs, (red circle) R2 and (black crosses) R3 and R4.

3. Results

3.1 *Large-scale morphology*

At the start of the field campaign the beach was in an intermediate state, with a rhythmic bar and beach (RBB, Wright and Short, 1984). The cross-shore measurement array was located at an embayment in the shoreline, where the intertidal area consisted of a steep intertidal bar, coinciding with an embayment in the subtidal bar. North of the instrument array, at the location of P9 and P10, the intertidal bar was not yet fully welded to the shoreline and a runnel was present in between (Figures 1c and 3). During the first 12 days of the experiment, the intertidal bar further steepened and moved in the onshore direction. The development of the bar was similar alongshore, although the cross-shore location of the bar was coupled to the crescentic shoreline (Figure 3a). During the storm, the offshore directed transport of sand resulted in a flattening of the intertidal beach profile along the entire field site (Figure 3b), although alongshore variability remained in both the shoreline and the subtidal bar. The high water levels during the storm also resulted in a significant accretion of sand (approx. 0.5 m) on the upper beach (Figure 3b). During the subsequent low-energetic swell and low water levels in the last week of the study period, the mean water level rarely exceeded the bar crest, resulting in the reformation of an intertidal bar and a migration in the onshore direction (Figure 3c).

At day 6 of the campaign, the cross-shore bed profiles at the location of P6, P7, the cross-shore array, P9 and P10 (Figure 4a) show that the location and height of the subtidal bar crest were alongshore variable and lowest at the location of the cross-shore array. The distance between the subtidal bar and the shoreline decreased from the cross-shore array both to the north and to the south, reflecting the difference in subtidal bar depth. The location of the intertidal bar, between x = 140 – 170 m (Figure 3), was coupled with this water depth variation above the subtidal bar, as it was located most landward at the cross-shore array (see also Figure 1c).

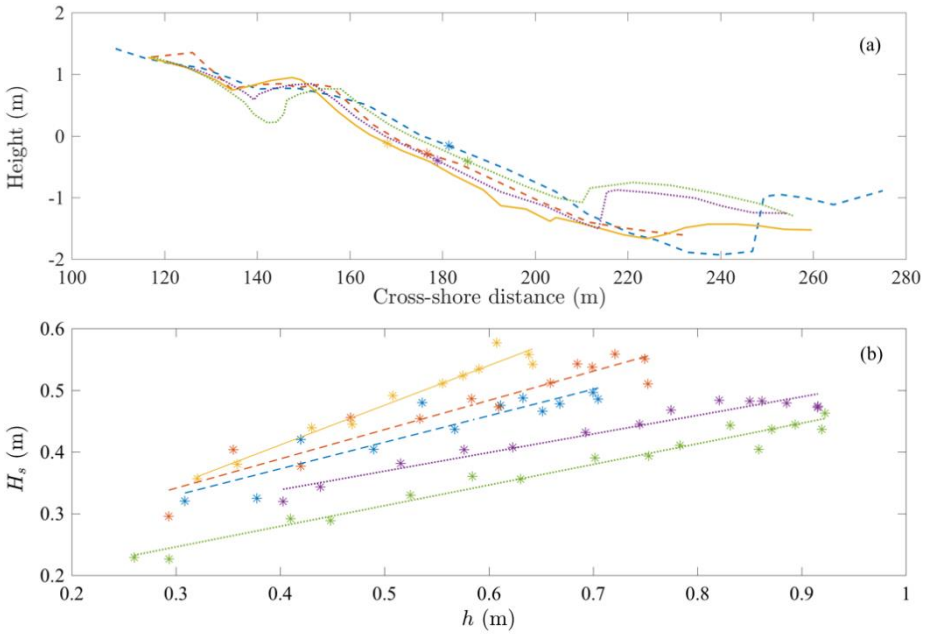

Figure 4. (a) Cross-shore bed profiles at (dashed blue) P6, (dashed red) P7, (solid yellow) the cross-shore array, (dotted purple) P9 and (dotted green) P10 at day 6 of the campaign. The dashed (dotted) bed profiles are located south (north) of the cross-shore array. The stars indicate the location of the pressure sensors. (b) Observed significant wave height (H_s) versus the water depth (h) for blocks of 30 minutes during one tidal cycle at the five alongshore locations. The lines show a linear fit through the observations of each instrument. Colors and line types are equal to (a).

In order to relate alongshore morphological variability in the intertidal zone with the incoming waves for different wave conditions and beach states, the wave data from the alongshore array of pressure sensors (P3 and P6-P10) was analyzed. As the bed level and thus the water depth varied between the locations of the sensors for a given time interval, observed H_s at the alongshore spaced PTs could not be directly compared.

To remove this additional variation in wave height, wave heights at a specific water depth can be compared at each alongshore location during a tidal cycle, through linear regression. Figure 4b shows an example of observed H_s versus h during an entire tidal cycle on day 6 of the campaign. Observed H_s at P3 (at the cross-shore array) was highest throughout the measured range in h and was up to 1.8 times higher than H_s at the more northern location P9, located landward of a shallower area in the subtidal bar. This agrees with the expected modulation in H_s driven by the alongshore depth variability in the subtidal bar. For low local h, the observed H_s shows less difference between the sensors, as H_s becomes limited by the local water depth.

3.2 *Small-scale morphology*

The presence of bedforms can increase the turbulence intensity close to the bed and ejected turbulent vortices from the ripple crests can reduce the magnitude or even reverse the direction of the short-wave sand transport (e.g. van der Werf et al., 2007; Brinkkemper et al., 2017). Moreover, measurements in the shoaling zone of a dissipative beach (Miles and Thorpe, 2015) showed that migrating ripples can explain up to 15% of the total transport. Observations of the bed state and ripple characteristics are thus relevant to understand sand transport and morphodynamics.

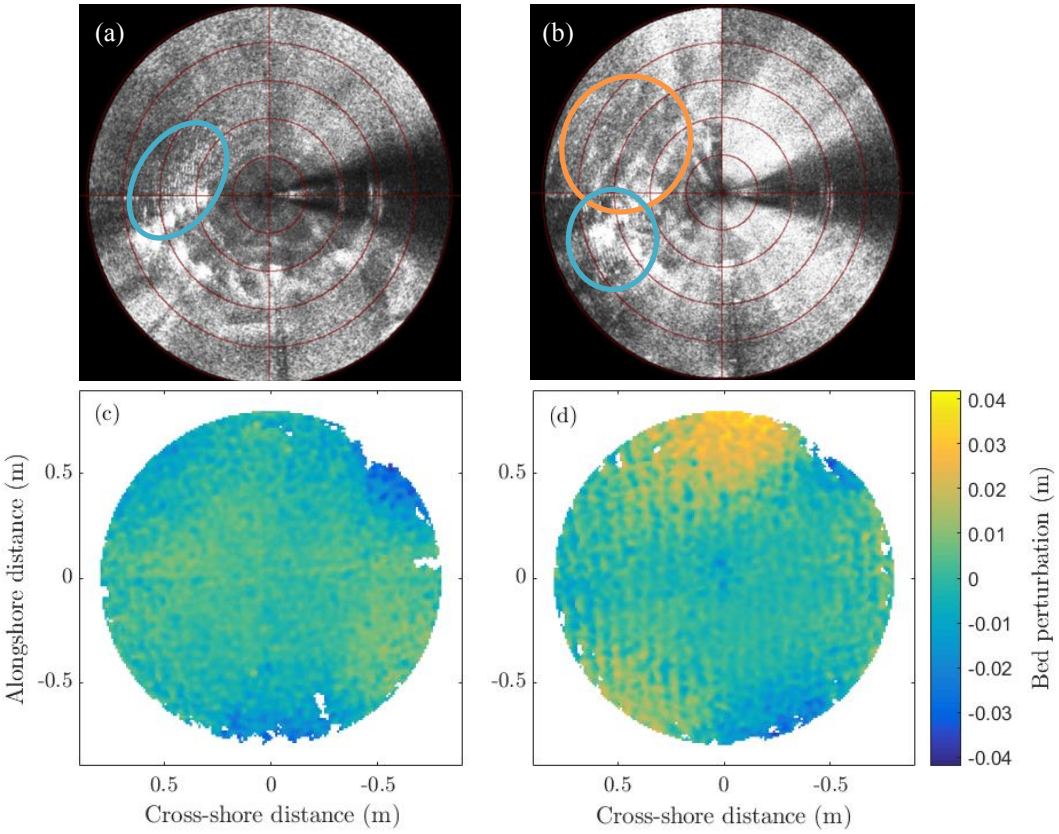

Figure 5. Two scans of the imaging sonar at R1 recorded at (a) September 21 at 06:20 AM and (b) September 23 at 07:40 AM and two processed scans of the profiling sonar at R2 at (c) September 21 at 06:00 AM, and (d) September 22 at 7:30 PM. The landward side is located at the right of the images. The V-shaped frame holding the main instrument suite at R1 can be seen at about 260 degrees in the image (a) and (b), wave ripples and mega-ripples are seen in the blue and orange encircled areas, respectively. The dark-red circles in (a) and (b) indicate a spacing of 1 m.

The mobility number ψ, here calculated as $\psi = u_m^2/(s\text{-}1)gD_{50})$ with u_m the vector product of the maximum orbital velocity, is often used to predict the bed state and ripple characteristics (e.g. Hay, 2011). Recent field measurements by Larsen et al. (2015) showed a transition from wave ripples to mega-ripples when ψ > 240, in contradiction with earlier measurements which show the bed to be flat for these conditions (Dingler and Inman, 1976). Here, we show some examples of bedform observations including raw data collected with the imaging sonar at R1 and processed data from the profiling sonar at R2 (Figure 5). The measured bed elevations at R2 were interpolated, using a second-order loess interpolator, to a grid with 0.01 m spacing using $l_x = l_y = 0.04$ m, and subsequently detrended ($l_x = l_y = 3.5$ m) to remove the large-scale morphology (Ruessink et al., 2015).

The observations collected during the first week of the campaign show a continuous presence of ripples at R1, wave ripples, mega-ripples, or both, and wave ripples or a flat bed at R2. In the morning of September 21, wave ripples with an orientation parallel to the shoreline were present at R1 (Figure 5a) while the bed was flat at R2 (Figure 5c). The mobility number during this high tide increases from around 200 at R1 to 240 at R2 (Figure 6c) and thus confirms earlier findings that ripples disappear when ψ > 240. While Northeast-Southwest orientated mega-ripples, with superimposed wave ripples, were present at R1 during the high tide at September 23 (Figure 5c), ψ was slightly lower than for the scan without mega-ripples. Scans from the collocated profiling sonar show that these mega-ripples, with a length of around 0.8 m, are 0.05-0.06 m in height. The orientation of the wave ripples is now slightly oblique in respect to the shoreline, which agrees with the change in wave direction (Figure 2c). Low mobility numbers at R2 also resulted in wave ripple formation (Figure 5d), ripple length and height in the scan from September 22 were around 0.06 and 0.02 m, respectively.

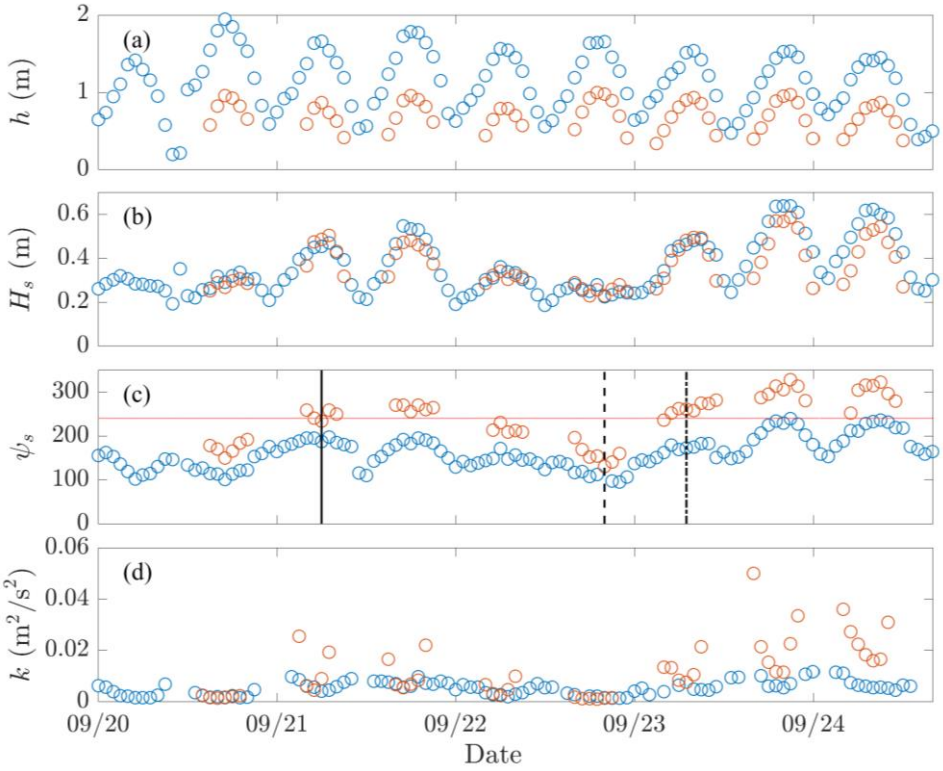

Figure 6. (a) Water depth h, (b) significant waveheight H_s, (c) mobility number ψ and (d) turbulent kinetic energy k, at around 0.15 m above the bed, at (blue) R1 and (orange) R2, during the first week of the campaign. The horizontal line in (c) indicates ψ=240, the vertical lines indicate the moments the ripple scans in (solid) Figures 5a,c (dashed) Figure 5d and (dashed-dotted) Figure 5b were recorded.

3.3 *Turbulence*

Previous measurements beneath irregular shoaling and breaking waves showed an increase of the turbulent kinetic energy k with relative waveheight (H_s/h) and a shift from a vertical profile increasing towards the bottom to a vertical profile increasing towards the surface (e.g. Grasso et al., 2012). These findings were based on turbulence observations collected on one cross-shore location and the variability in H_s/h was thus caused by the offshore wave conditions. The turbulence measurements presented here were collected at two cross-shore locations and thus give a better insight in the cross-shore variability in turbulence characteristics.

Figure 6 shows the variability in hydrodynamics during the first week, when measurements were collected at both locations. The tidal water depth variations (Figure 6a) drive variations in H_s (Figure 6b), as with lower water levels more waves start breaking at the subtidal bar. The turbulent kinetic energy k at 0.15 m above the bed, which was estimated from the ADV measurements using the differencing method (Feddersen and Williams, 2007), also shows a variation with h at R1 (Figure 6d), with higher k during low tide. The magnitude of H_s at R1 and R2 is similar until September 23, indicating that both rigs are located seaward of the surf zone during high water. The magnitude of k during those days is very similar at the two rigs during high tide, which shows that turbulence levels are relatively constant throughout the shoaling zone. In this period k is only occasionally higher at R2 during rising and falling tide, as it is then located in the surf zone. During the last two high tides shown, H_s decreases from R1 to R2 and waves thus dissipate energy due to breaking. Here, k levels significantly increase at the inner rig R2. Further analyses will focus on whether this breaking-induced turbulence can affect short-wave sand transport.

4. Conclusions

Detailed measurements of hydro- and morphodynamics were collected in the intertidal zone at the beach of Vejers. The campaign included two periods of accretive conditions with an onshore directed migration of the intertidal bar. These periods were characterized by low-moderate energetic conditions, while the intertidal beach profile was flattened during a storm, with high waves and water levels, in between these two periods. The intertidal morphology was alongshore variable throughout the campaign, especially during periods with an onshore migrating intertidal bar. Observations of the wave height at different alongshore locations along the low water line showed that differences in the intertidal morphology could be linked with alongshore differences in incoming wave energy due to a water depth variability over the crest of the subtidal bar. Measurements at two cross-shore locations show wave ripples to be present when the mobility number is below 240, a similar relation with the mobility number for the formation and disappearance of the observed mega-ripples was not found. Turbulence levels are relatively constant over distance in the shoaling zone and significantly increase in the surf zone. It is anticipated that this extensive dataset will enhance our understanding of the hydro- and morphodynamics in shallow water and in particular the processes involved in the onshore directed migration of longshore bars during low-moderate energetic conditions.

Acknowledgements

This field campaign would not have been possible without the support of the technicians from the University of Copenhagen (Paul Christiansen, Mathias Madsen and Per Freiberg) and Utrecht University (Marcel van Maarseveen, Henk Markies and Arjen van Eijk). Gabriel Herbst from Herbst Environmental Science is acknowledged for the technical support for the sonars at R1.

References

Aagaard, T., Hughes, M., Møller-Sørensen, R. and Andersen, S., 2006. Hydrodynamics and sediment fluxes across an onshore migrating intertidal bar. *Journal of Coastal Reseach,* 22(2): 247-295. doi: 10.2112/04-0214.1

Aagaard T. and Kroon A. 2007. Mesoscale behaviour of multiple-bar systems – net onshore or net offshore migration.

Proceedings Coastal Sediments '07, American Society of Civil Engineers; 2124–2136.

Aagaard, T., Kroon, A., Hughes, M.G. and Greenwood, B., 2008. Field observations of nearshore bar formation. *Earth Surface Processes and Landforms* 33, 1021-1032, doi: 10.1002/esp.1599

Aagaard T. and Vinther, N., 2008. Cross-Shore Currents in the Surf Zone: Rips or Undertow? *Journal of Coastal Research*, 24(3): 561-570. doi: 10.2112/04-0357.1

Aagaard, T. and Hughes, M.G., 2010. Breaker turbulence and sediment suspension in the surf zone. *Marine Geology*, 271 (3-4), 250-259, doi:10.1016/j.margeo.2010.02.019.

Aagaard, T., 2011. Sediment transfer from beach to shoreface: The sediment budget of an accreting beach on the Danish North Sea Coast. *Geomorphology,* 135: 143-157, doi: 10.1016/j.geomorph.2011.08.012

Aagaard, T. and Jensen, S.G., 2013. Sediment concentration and vertical mixing under breaking waves. *Marine Geology*, 336, 146-159, doi:10.1016/j.margeo.2012.11.015.

Brinkkemper, J.A., Lanckriet, T., Grasso, F., Puleo, J.A. and Ruessink, B.G., 2016. Observations of turbulence within the surf and swash zone of a field-scale sandy laboratory beach. *Coastal Engineering*, 113, 62–72, doi:10.1016/j.coastaleng.2015.07.006.

Brinkkemper, J.A., de Bakker, A.T.M. and Ruessink, B.G., 2017. Intrawave sand suspension in the shoaling and surf zone of a field-scale laboratory beach, *Journal of Geophysical Research: Earth Surface*, 122, doi:10.1002/2016JF004061.

Dingler, J.R. and Inman, D.L., 1976. Wave-formed ripples in nearshore sands. *Proc. 15th Int. Conf. Coastal Eng*, Am.Soc. Civil Eng., pp. 2109–2126 (New York)

Castelle, B., Ruessink, B.G., Bonneton, P., Marieu, V., Bruneau, N. and Price, T.D., 2010. Coupling mechanisms in double sandbar systems. Part 2: impact on alongshore variability of inner-bar rip channels. Earth Surface Processes and Landforms, 35(7), pp.771-781.

Falqués, A., Coco, G. and Huntley, D.A., 2000. A mechanism for the generation of wave-driven rhythmic patterns in the surf zone. Journal of Geophysical Research: Oceans, 105(C10), pp.24071-24087.

Feddersen, F., and Williams, A.J., 2007. Direct estimation of the Reynolds stress vertical structure in the nearshore. *Journal of Atmospheric and Oceanic Technology*, 24 (1), 102-116.

Gallagher, E.L., Elgar, S. and Guza, R.T., 1998. Observations of sand bar evolution on a natural beach. *Journal of Geophysical Research, 103.C2*: 3203-3215.

Grasso, F., Castelle, B. and Ruessink, B.G. 2012. Turbulence dissipation under breaking waves and bores in a natural surf zone. *Continental Shelf Research* 43, 133-141.

Hansen, A.B., Carstensen, S, Christensen, D.F. and Aagaard, T., 2017. Performance of tilt current meter in the surf zone. *Proceedings of Coastal Dynamics '17,* Helsingor, Denmark

Hay, A.E., 2011. Geometric bed roughness and the bed state storm cycle. *Journal of Geophysical Research* 116 (C04017), doi:10.1029/2010JC006687

Larsen, S.M., Greenwood, B. and Aagaard, T., 2015. Observations of megaripples in the surf zone. *Marine Geology*, 364, 1-11, 10.1016/j.margeo.2015.03.003.

Miles, J. and Thorpe, A., 2015. Bedform contributions to cross-shore sediment transport on a dissipative beach, *Coastal Engineering*, 98, 65–77, doi:10.1016/j.coastaleng.2015.01.007.

Nadaoka, K., Ueno, S. and Igarashi, T., 1988. Sediment suspension due to large scale eddies in the surf zone, in *Proceedings of the 21st International Conference on Coastal Engineering*, pp. 1646-1660.

O'Donoghue, T. and Wright, S., 2004. Flow tunnel measurements of velocities and sand flux in oscillatory sheetflow for well-sorted and graded sands, Coastal Engineering, 51 (11-12), 1163-1184, doi:10.1016/j.coastaleng.2004.08.001.

Price, T.D., Ruessink, B.G. and Castelle, B., 2014. Morphological coupling in multiple sandbar systems-a review. Earth Surface Dynamics, 2(1), 309, doi:10.5194/esurf-2-309-2014

Radermacher, M., Thackeray, Z, de Schipper, M, Gordon, L., Chrystal, C., Leuci, R and Reniers, A., 2015. Tilt current meter array: Field validation. *E-proceedings of the 36th IAHR World Congress*, The Hague, the Netherlands.

Ribberink, J.S. and Al-Salem, A.A., 1994. Sediment transport in oscillatory boundary layers in cases of rippled beds and sheetflow. *Journal of Geophysical Research*, 99 (C6), 12,707-12,727.

Ruessink, B. G., 2010. Observations of turbulence within a natural surf zone. *Journal of Physical Oceanography*, 40(12), 2696–2712, doi:10.1175/2010JPO4466.1.

Ruessink, B.G., Brinkkemper, J.A. and Kleinhans, M.G., 2015. Geometry of wave-formed orbital ripples in coarse sand. *Journal of Marine Science and Engineering*, 3(4), 1568–1594, doi:10.3390/jmse3041568.

Silva, P.A., Abreu, T., Van Der A, D.A., Sancho, F., Ruessink, B.G, Van der Werf, J. and Ribberink, J.S., 2011. Sediment transport in nonlinear skewed oscillatory flows: Transkew experiments, *Journal of Hydraulic Research*, 49 (sup1), 72-80, doi: 10.1080/00221686.2011.592681.

Sunamura, T and Takeda, I., 1984. Landward migration of inner bars. In: B. Greenwood and R.A. Davis, Jr. (Editors), Hydrodynamics and Sedimentation in Wave-Dominated Coastal Environments. *Marine Geology*, 60: 63--78.

van der A, D.A., O'Donoghue, T. and Ribberink, J.S., 2009. Sheetflow sand transport processes in oscillatory

flow with acceleration skewness. *Paper 133 in Proc.Coastal Dynamics '09, World Sci., Singapore.*

van der Werf, J.J., Doucette, J.S., O'Donoghue, T. and Ribberink, J.S., 2007. Detailed measurements of velocities and suspended sand concentrations over full-scale ripples in regular oscillatory flow. *Journal of Geophysical Research*, 112(F02012), doi: 10.1029/2006JF000614.

van Rijn, L.C., Tonnon, P.K. and Walstra, D.J.R., 2011. Numerical modelling of erosion and accretion of plane sloping beaches at different scales. *Coastal Engineering* 58, 637–655, 10.1016/j.coastaleng.2011.01.009.

Watanabe, A. and Sato, S., 2004. A sheetflow transport rate formula for asymmetric, forward-leaning waves and currents, in *Proceedings of the 29th International Conference on Coastal Engineering*, pp. 1703-1714.

Wright, L.D. and Short, A.D., 1984. Morphodynamic variability of surf zones and beaches: a synthesis. Marine Geology, 56(1-4), pp.93-118.